Near-field measurement and four-wave mixing in single-polarization elliptical multimode VCSELs

Journal of Physics: Photonics

OPEN ACCESS

RECEIVED
25 July 2025

REVISED
2 October 2025

ACCEPTED FOR PUBLICATION
19 October 2025

PUBLISHED
6 November 2025

PAPER

Near-field measurement and four-wave mixing in single-polarization elliptical multimode VCSELs

Cristina Rimoldi[1,2,4], **Marco Novarese**[2,4], **Lorenzo Luigi Columbo**[2], **Sebastian Romero García**[3], **Christian Raabe**[3] and **Mariangela Gioannini**[1,*]

[1] CNR-Istituto Nazionale di Ottica (CNR-INO), Sesto Fiorentino (FI), Italy
[2] Dipartimento di Elettronica e Telecomunicazioni, Politecnico di Torino, Torino, Italy
[3] Cisco Optical, Nordostpark 12, Nuremberg, Germany
[4] The authors contributed equally to this work.
[*] Author to whom any correspondence should be addressed.

E-mail: mariangela.gioannini@polito.it

Keywords: semiconductor lasers, multimode VCSELs, elliptical oxide aperture, four-wave mixing, RIN, near-field measurement

Abstract

We investigate the impact of transverse mode coupling caused by four-wave mixing (FWM) in elliptical multimode vertical cavity surface emitting lasers (VCSELs) with polarization control. Our study includes relative intensity noise (RIN) and near-field measurements, with a particular focus on the near-field pattern of sidebands of the lasing modes observed in the optical spectrum. Our model, which includes coherent mode coupling via FWM and spatial hole burning, shows a very good agreement between numerical and experimental results, providing a detailed explanation of the fine spectral features observed in the optical and RIN spectra. These results identify the primary causes of RIN degradation in multimode VCSELs and highlight the importance of considering FWM when approaching the design of VCSELs for high-speed and datacom applications.

1. Introduction

Nowadays, vertical cavity surface emitting lasers (VCSELs) are widely employed in datacenter optical interconnects [1], where laser output powers of several mW and a wide modulation bandwidth for rates higher than 100 Gb s^{-1} are required. For this purpose, large aperture (>3 μm diameter) multi-mode VCSELs are employed [2], but, very often, quasi-circular oxide aperture multimode VCSELs show poor relative intensity noise (RIN) performance. Further, the degradation of the RIN spectrum impacts the eye diagram performance of the laser when modulating at high speed in OOK NRZ or PAM4 modulation formats, thus limiting the transmission speed [3] of many VCSELs originally designed for high-capacity datacom. The authors of [3] present a detailed analysis of experimental RIN spectra, demonstrating how multimode and few-mode VCSELs with quasi-circular geometry show several spectral peaks in the RIN leading to unacceptable increases of the RIN integrated over the receiver bandwidth. These features are empirically explained in [3] as a consequence of a generic mode beating between quasi-degenerate modes separated in frequency by only a few GHz, but there is a significant knowledge gap that hinders the clear understanding of the origin of these peaks. The relationship between modal frequency separation and peaks in the RIN is non-trivial [4] and impossible to explain from a pure 'black box' device characterization perspective [3]. For this reason, an in-depth analysis of the RIN is needed to provide a theoretical framework (supported by experiments) that can give useful insights when approaching the design of novel optimized VCSELs.

In a rigorous study that we recently published [5], we showed that such RIN peaks can be observed even in multimode polarization controlled VCSELs (i.e. linearly emitting only in one polarization). In this case, our numerical model, accounting for coherent frequency mixing and spatial hole burning, demonstrated that these RIN peaks are a non-trivial consequence of four-wave mixing (FWM) between transverse lasing modes, mediated by carrier beating. Furthermore, in our paper [5], we derived theoretical analytical expressions to predict the RIN peak frequency and showed that the overlapping integral of

the spatial profiles of the transverse modes involved in the FWM process plays a very important role in determining which are the frequency mixing components that actually appear in the RIN. Additionally, if the device under consideration is not specifically designed to emit linearly polarized light, other RIN peaks are added to the optical spectrum; these are due to the beating of the same transverse mode emitting in the two polarizations [6]. Note that, due to the limited bandwidth of the measurement setup, RF power/RIN peaks were observed in these papers [3, 6] for frequencies up to 16 GHz and 40 GHz, respectively.

The aims of the work that we present in this paper are:

- prove, through experimental characterization of the VCSEL, that FWM among transverse modes is possible and that it can be measured in the optical spectrum as optical sidebands (at different frequencies), associated with specific lasing modes. This approach enables the assessment of frequency beating components beyond the bandwidth limitations of present-day RIN measurement setups which are typically limited to ≈40 GHz;
- show that, by increasing the bias current, the number of optical sidebands increases along with the number of lasing transverse modes and that our analytical expressions based on FWM theory can predict the optical frequency of the sidebands and their near-field patterns, as also measured;
- demonstrate the relation between optical FWM sidebands and RIN peaks;
- analyze how the RIN evolves for increasing bias currents, up to the case where seven transverse modes are lasing, and prove that our analytical approach can also perfectly track this evolution.

In this work, we characterize an 850 nm multimode VCSEL with an elliptical oxide aperture, which has been designed to effectively suppress one polarization. Our experimental characterization makes use of a lensed fiber near-field measurement to assess the mode spatial profiles, as well as the spatial profiles of the spectral optical sidebands. In previous publications [5], a few preliminary near-field measurements based on the use of diffraction gratings (to separate transverse modes in space) and a camera (for acquisition) were presented on similar VCSELs. However, the employment of diffraction gratings limited the results in terms of (i) frequency resolution and (ii) transverse spatial resolution [7]. Further, (iii) the employment of diffraction gratings attenuates the fields, making it possible to visualize only the main lasing modes on the CCD camera. As a result, all information about the sidebands is lost.

A possible pathway to tackle the degradation in the RIN is considering different aperture shapes [8] to break the cavity symmetry: for example, by adopting an elliptical oxide aperture, the frequency separation of transverse modes of the same order (which would otherwise be frequency degenerate in the circular case) is increased and the RIN spectral peaks could move to very high frequencies, filtered out by the receiver [5]. To aid these designs, this work provides a few rules for identifying beating frequencies in elliptical oxide aperture VCSELs to potentially obtain an improved laser performance, based solely on the frequency, threshold, and spatial profile of lasing modes resulting from the VCSEL experimental characterization or electromagnetic simulations for an arbitrary epilayer structure.

2. Experimental setup and device characterization

To accurately locate modes and sidebands in optical frequency, we record the total optical spectrum through a coupling unit as illustrated in figure 1(a): using a two-lens setup, the light from the VCSEL is first collimated and then focused into a multimode fiber, connected to a high-resolution Optical Spectrum Analyzer (OSA, Yokogawa AQ6370E-20/Z) with a resolution bandwidth of 4 GHz. Figure 1(b) shows the optical spectrum with a bias current of $I = 8$ mA, where the x-axis has been shifted so that the frequency of the fundamental mode C_1 emitting at 858 nm is set to 0 GHz.

We denote the modes as C_1 to C_7, starting from the fundamental mode up to the higher-order modes [5], while S_1 to S_{11} are the labels of the sidebands appearing in the optical spectrum, from lower (i.e. near the fundamental mode) to higher frequencies. The values of the mode C_m detunings with respect to C_1 are: $\Delta\nu_{1-7} = \Delta\omega_{1-7}/2\pi$ =0, 212, 300, 452, 527, 616, 691 GHz.

The lensed fiber setup is shown in figure 1(c). Here, a single mode lensed fiber, designed for 850 nm, with a spot size of 1.3 μm at a working distance of 11.2 μm, is used to measure the near-field optical spectra via scanning the xy-plane on a circular area of a 10 μm radius. For each point of the grid (with $\Delta x = 800$ nm and $\Delta y = 800$ nm) we acquire the optical spectrum; by post-processing the data, we can reconstruct the near-field pattern of the modes C_m and of the sidebands S_i. With this technique we can

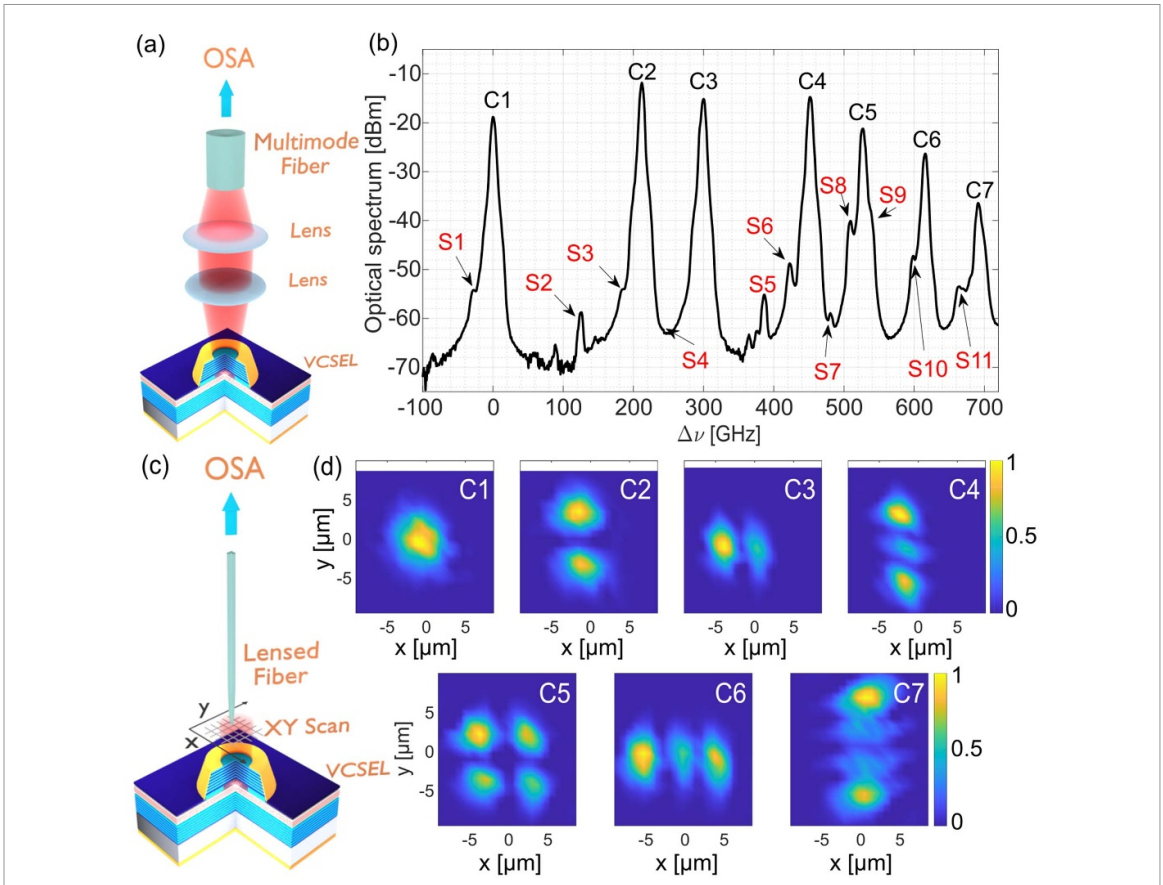

Figure 1. (a) Schematic of the coupling unit setup. (b) Full optical spectrum as a function of the detuning with respect to the fundamental mode measured with the coupling unit setup for $I = 8$ mA, with labeled modes, C_1–C_7, and sidebands, S_1–S_{11}. (c) Schematic of the lensed fiber setup for near field measurements. (d) Near-field spatial profiles of different modes, C_1 to C_7, obtained from the scan.

determine the power distribution as a function of the position in the xy-plane with an accuracy much larger than other methods involving diffraction gratings or CCD camera [9].

The spatial profiles of the lasing modes C_1 to C_7 acquired through this method are shown in figure 1(d); near-field patterns of the sidebands will be discussed in the following. These spatial profiles are the result of a deconvolution procedure that we followed to account for the convolution of the near-field profile after the VCSEL, referred to as the object image, with the lensed fiber beam spot, which acts as the Point Spread Function (PSF) [10]. The PSF generally represents the response of an optical system to a point object. In our case, we account for both the distortion caused by the lensed fiber movement during the scan and the transverse profile of the beam spot of the lensed fiber. The former is addressed using a motion-based PSF, followed by a deconvolution procedure employing the Wiener filter algorithm [11]. The resulting spatial profile undergoes an additional deconvolution process using a maximum likelihood algorithm [12], where the PSF is modeled as a disk with a radius equal to the lensed fiber spot size.

Figure 2(a) presents the optical spectra map as a function of detuning relative to the fundamental mode for currents ranging from 2 mA to 10 mA as measured with the coupling unit setup in figure 1(a). The positions of the sidebands S_{1-11} are highlighted to illustrate how they emerge as the current increases and other additional modes start to lase. This trend is further clarified in figures 2(b)–(d), which show the optical spectra with increasing currents, specifically $I = 3$ mA, 6 mA, and 9 mA. The setup in figure 1(a) was also used to acquire RIN spectra via a 40 GHz RIN measurement system (SYCATUS, A0010A-040), consisting of a signal analyzer (Keysight Technologies N9030A-544), an optical receiver (SYCATUS), and a digital multimeter (Keysight Technologies 34 461A). Results of the RIN measurements will be discussed in the following sections.

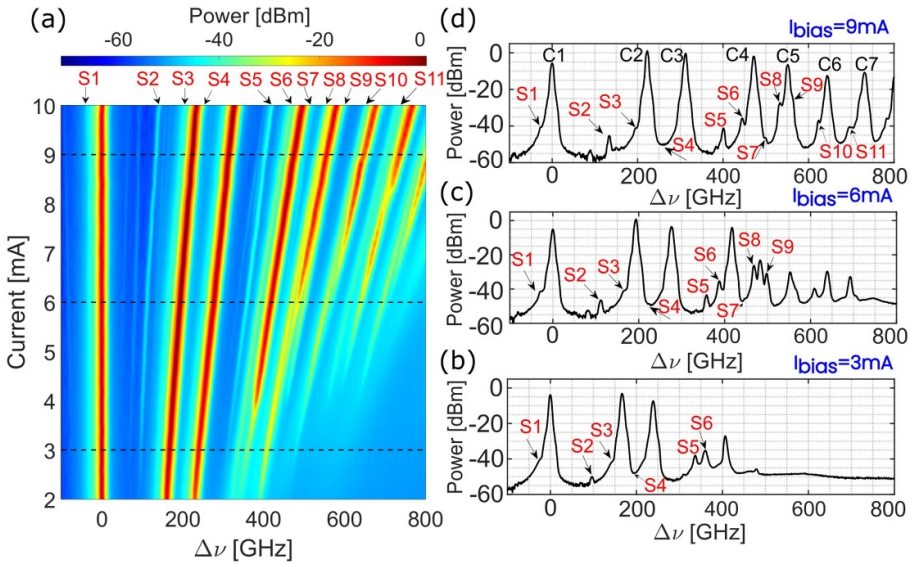

Figure 2. (a) Map of the optical spectra for different detunings and currents, measured with the coupling unit. Black dashed lines indicate cuts of the optical spectra for bias currents of (b) 3 mA, (c) 6 mA, and (d) 9 mA. Modes and sidebands are labeled as in figure 1(b).

3. Model and simulations

We reproduce and interpret the experimental results using the model, previously presented by the authors [5], based on the expansion of the transverse electric field $E(\rho,\phi,t)$ on the orthonormal basis of real Hermite Gauss modes $C_m(\rho,\phi)$ (of which we report the analytical form up to $m=7$ in appendix A) and on the expansion of the carrier density $N(\rho,\phi,t)$ on an orthonormal basis of Gauss Laguerre functions [5]. Differently from other approaches in literature, this model accounts for coherent frequency mixing between modes, as well as spatial hole burning. The complete dynamical model [5] mainly requires, as input parameters, the size of the VCSEL oxide aperture, the detuning frequency and threshold of each of the transverse lasing modes (resulting in different photon lifetimes $\tau_{p,m}$). The remaining parameters, such as the differential gain g_N, the longitudinal confinement factor Γ, the α factor, and the carrier diffusion, are taken from literature or obtained through experimental fitting. With this model we can simulate L-I curves, optical spectra, and RIN spectra. Our simulations are in good agreement with the experimental findings and allow to interpret the formation and growth of the sidebands in the optical spectra and the peaks observed in the RIN.

In figure 3, we demonstrate such an agreement by reporting the experimental (green) and numerical (black) RIN for $I_{\text{bias}} = 7$ mA (a), as well as the experimental and numerical optical spectra at the same current (b), obtained with $m=5$ lasing modes. The parameters used for these results are the same as in previous publications [5] except for the parameters reported in table 1. Here, we can clearly observe that the model is able to describe the 3 high-intensity peaks occurring in the RIN, as well as the sidebands observed in the optical spectrum.

A reduced version of the model, obtained under reasonable approximations, neglecting the effects of gain compression, carrier diffusion, and by assuming that carriers are fast enough to follow the optical electric field, allows to describe the VCSEL solely through a set of m ordinary differential equations (neglecting the contribution of spontaneous emission)

$$\frac{\mathrm{d}\tilde{E}_m}{\mathrm{d}t} = -\frac{1+i\alpha}{2\tau_{p,m}}\tilde{E}_m \tag{1}$$

$$+\tilde{g}\Lambda\left[1-\gamma_{mmmm}\frac{|\tilde{E}_m|^2}{E_s^2}-2\sum_{n\neq m}\gamma_{mmnn}\frac{|\tilde{E}_n|^2}{E_s^2}\right]\tilde{E}_m \tag{2}$$

$$-\tilde{g}\Lambda\sum_{n,r,l;\omega_{nm}+\omega_{lr}\neq 0}\gamma_{mnrl}\frac{\tilde{E}_n\tilde{E}_l\tilde{E}_r^*}{E_s^2}\mathrm{e}^{\mathrm{i}(\omega_{nm}+\omega_{lr})t} \tag{3}$$

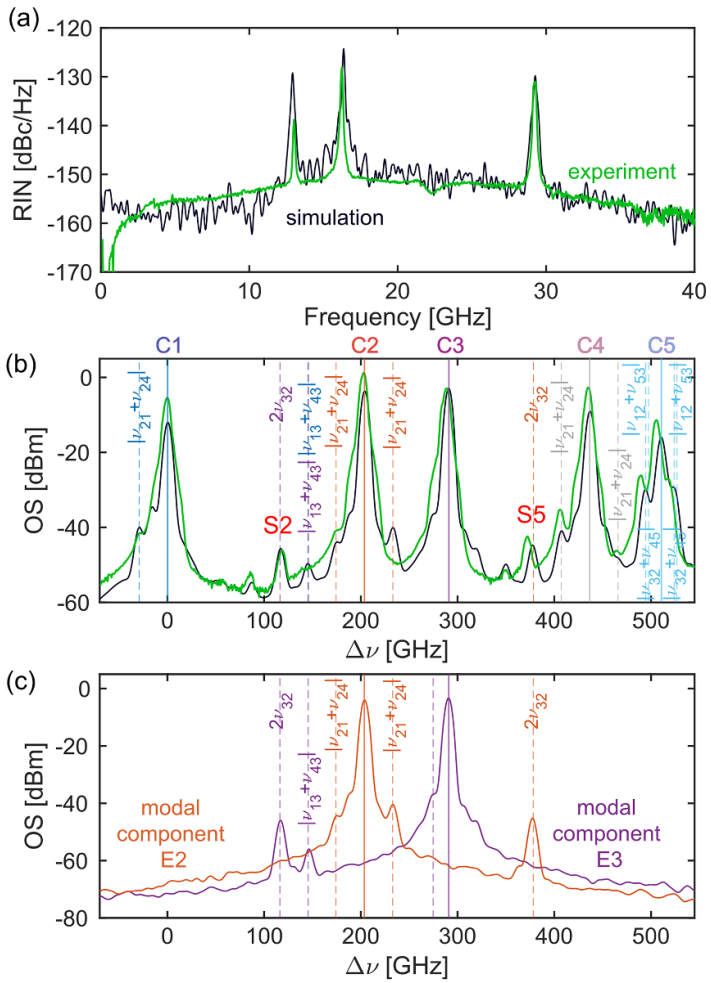

Figure 3. (a) Experimental (in green) and numerical (in black) RIN at $I_{\text{bias}} = 7$ mA. (b) Experimental (green) and numerical (black) optical spectrum. Vertical solid lines of different colors highlight lasing modes C_{1-5}. Vertical dashed lines highlight sidebands of the mode of the same color. Sideband labels indicate the associated beating frequency. (c) Optical spectrum of the modal component $E_2(t)$ (in orange) and $E_3(t)$ (in violet).

Table 1. Model parameters.

Quantity	Definition	Value	Unit
G_N	$g_N v_g$	5×10^{-6}	$\text{cm}^3\ \text{s}^{-1}$
$\tau_{p,1}$	Photon lifetime mode C1	1.8	ps
$\tau_{p,2}$	Photon lifetime mode C2	1.34	ps
$\tau_{p,3}$	Photon lifetime mode C3	1.25	ps
$\tau_{p,4}$	Photon lifetime mode C4	0.94	ps
$\tau_{p,5}$	Photon lifetime mode C5	0.9	ps
V	Active region volume	5.93×10^{-13}	cm^3
ϵ	gain compression factor	1.5×10^{-23}	m^3

where $\tilde{E}_m(t)$ is the electric field modal component such that $E(\rho,\phi,t) = \sum_m \tilde{E}_m(t) e^{i\omega_m t} C_m(\rho,\phi)$, with ω_m being the angular frequency detuning of mode m with respect to the fundamental mode C_1, obtained from the experiment. The complex gain term is $\tilde{g} = \Gamma G_N(1+i\alpha)/2$, the normalized current term is $\Lambda = \eta_i I/eV - N_0/\tau_e$, and $1/E_s^2 = n_g^2 \epsilon_0 G_N \tau_e / 2\hbar\omega_0$ (for other parameter definitions, refer to previous publications [5]).

In equations (1)–(3), term (2) accounts for self- and cross-saturation and term (3) describes the FWM process, mediated by carrier beating [5], causing an oscillation in both amplitude and phase of mode C_m at the beating frequency $\omega_{nm} + \omega_{lr} = \omega_n - \omega_m + \omega_l - \omega_r$. The intensity of such oscillations depends on the power of the other modes (n, l, and r) and on the coefficient γ_{mnrl}, which accounts for

the spatial profile of the competing transverse modes through the integral term

$$\gamma_{mnrl} = \int_0^{\infty} \int_0^{2\pi} C_m(\rho,\phi)\, C_n(\rho,\phi)\, C_r(\rho,\phi)\, C_l(\rho,\phi)\, \rho \mathrm{d}\rho \mathrm{d}\phi. \tag{4}$$

It is very important to realize that symmetry considerations on the mode transverse profiles allow to cancel out many of the terms in (3). In table 3 in appendix B, we report all non-null frequency beating terms resulting from the interaction of the first 7 Hermite-Gauss modes $C_m(\rho,\phi)$, highlighting those falling within a 200 GHz window for most common elliptical oxide aperture VCSELs.

We highlight that we expect the beating frequencies appearing in the differential equation for $\tilde{E}_m$ to occur as sidebands of the modes involved in the beating in the optical spectrum. Indeed, the optical spectrum is numerically calculated as the Fourier transform ($\mathcal{F}$) of the optical electric field then filtered by the OSA filter and, defined as

$$\mathrm{OS}(\lambda_k) = \int_{\lambda_R} \int_0^{\infty} \int_0^{2\pi} \left| \mathcal{F}\left[\left(\sum_m \tilde{E}_m(t)\, \mathrm{e}^{\mathrm{i}\omega_m t} C_m(\rho,\phi) \right) H_{OSA}(\lambda,\lambda_k) \right] \right|^2 \rho \mathrm{d}\rho \mathrm{d}\rho \mathrm{d}\phi\, \mathrm{d}\lambda$$

where the sum in parentheses is the total electric field, $H_{OSA}(\lambda,\lambda_k)$ is the OSA filter function, λ_k is the wavelength sampling points, and λ_R is the integration region associated with the instrument resolution bandwidth. Further, we expect such beating frequencies to occur as peaks in the RIN since the total output power measured at the photodiode (integrated over the transverse plane) is $P_{\mathrm{tot}} = \sum_m |\tilde{E}_m(t)|^2$ [5] and the dynamics of the total power follows

$$\frac{\mathrm{d}P_{\mathrm{tot}}(t)}{\mathrm{d}t} = \sum_m \frac{\mathrm{d}|\tilde{E}_m|^2}{\mathrm{d}t} = \sum_m \left(\tilde{E}_m(t) \frac{\mathrm{d}\tilde{E}_m^*(t)}{\mathrm{d}t} + \tilde{E}_m^*(t) \frac{\mathrm{d}\tilde{E}_m(t)}{\mathrm{d}t} \right). \tag{5}$$

as numerical confirmed in the case of two lasing modes (C_2 and C_3 lasing), in previous publications [5].

In the following paragraphs, we will experimentally prove these two points, and show how the reduced model allows for the explanation and prediction of the spurious peaks in the experimental RIN and of sidebands in the experimental optical spectrum.

At $I_{\mathrm{bias}} = 7$ mA, the approximate frequency detuning values measured from the optical spectrum in figure 2(a) for the 5 lasing modes are $\Delta\nu_{m=1-5}$ =0, 203, 288, 434, 506 GHz. The uncertainty in the measured values accounts for the frequency repeatability of the OSA, which is approximately 2 GHz at 850 nm. Therefore, our simplified model predicts the following beating terms, to be compared with the RIN high intensity peaks in figure 3(a): (i) $\nu_{45} + \nu_{32} = 13$ GHz, explaining the frequency location of the first RIN peak, (ii) $\nu_{53} + \nu_{12} = 15$ GHz, explaining the RIN peak at 16.2 GHz, and (iii) $\nu_{42} + \nu_{12} = 28$ GHz, explaining the RIN peak at 29.3 GHz.

Although the experimental RIN measurement is limited by the 40 GHz bandwidth of the photodiode, the optical spectrum at 7 mA in figure 3(b) reveals sidebands due to further FWM components. This confirms further our theoretical prediction that RIN peaks and optical sidebands are generated through the FWM process. Note that these sidebands, displayed in dashed lines of different colors, are labeled with the frequency distance (or beating frequency) calculated from the mode C_m of the same color. For example, the purple sideband S_2 is at $2\nu_{32}$ from C_3: this means that it originates from the beating of mode C_3 at the frequency $2\nu_{32}$ (and similarly for the orange sideband at $2\nu_{32}$ from mode C_2).

In the same way, we can observe sidebands (dashed lines) due to beating at $|\nu_{21} + \nu_{24}|$ around modes C_1 (in blue), C_2 (in orange) and C_4 (in gray). In this case, modes C_1, C_2, and C_4 oscillate at frequency $|\nu_{21} + \nu_{24}|$ due to nonlinear interaction among modes C_1, C_2, and C_4. Further sidebands are those around mode C_5, resulting from the contribution of beating frequencies $|\nu_{32} + \nu_{45}|$ and $|\nu_{12} + \nu_{53}|$ as well as a small numerical peak around 150 GHz resulting from the contribution of a sideband of C_3 at the beating frequency $|\nu_{13} + \nu_{43}|$ and a sideband of C_1 at the beating frequency $|\nu_{13} + \nu_{43}|$. Smaller peaks in the optical spectrum are the result of higher order effects neglected in the reduced model in equations (1)–(3). Further, we point out that additional FWM sidebands other than those shown in figure 3(b) might occur (see table 3) but the values of their superposition integral, in equation (4), and of the involved modal components $\tilde{E}_m$ are small enough that both in the numerical and in the experimental case, they end up below the (simulated or actual) instrument sensitivity. While most sidebands are located near the mode they refer to (e.g. sidebands in blue around mode C_1), it is interesting to notice that a sideband of C_2 appears at $\Delta\nu \approx 380$ GHz and a sideband of C_3 develops around $\Delta\nu \approx 115$ GHz. To further highlight this aspect via the post-processing of the simulation results, instead of simply considering the total optical spectrum calculated from $E(\rho,\phi,t) = \sum_m E_m(t) C_m(\rho,\phi)$, as in figure 3(b),

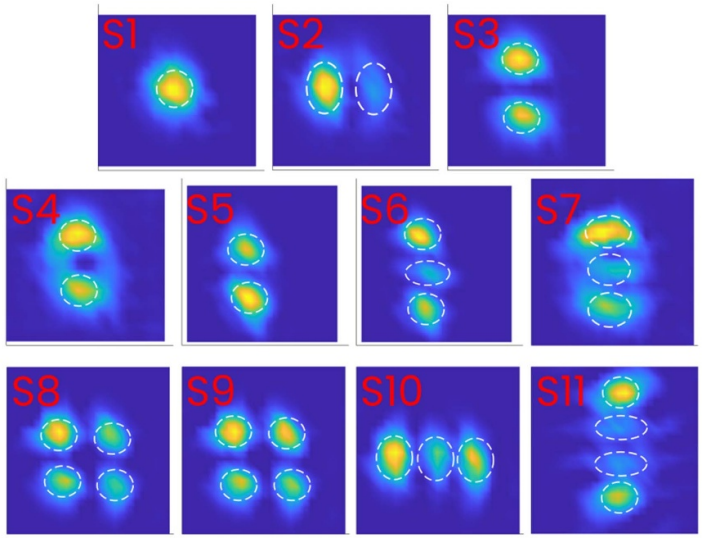

Figure 4. Spatial profiles of the sidebands observed in the spectrum shown in figure 1(b).

Table 2. Predicted and measured values of the beating frequencies resulting in sidebands, with respect to the fundamental mode C1 frequency.

Sidebands	Coeff.	Predicted [GHz]	Exp. [GHz]
S_1	γ_{1224}	$\nu_1 \boxed{-(\nu_{21}+\nu_{24})} = -28$	–27
S_2	γ_{2233}	$\nu_3 \boxed{-2(\nu_{23})} = 124$	126
S_3	γ_{1224}	$\nu_2 \boxed{-(\nu_{21}+\nu_{24})} = 184$	186
S_4	γ_{1224}	$\nu_2 \boxed{+(\nu_{21}+\nu_{24})} = 240$	243
S_5	γ_{2233}	$\nu_2 \boxed{+2(\nu_{23})} = 388$	387
S_6	γ_{1224}	$\nu_4 \boxed{-(\nu_{21}+\nu_{24})} = 424$	423
S_7	γ_{1224}	$\nu_4 \boxed{+(\nu_{21}+\nu_{24})} = 480$	481
S_8	γ_{1235}	$\nu_5 \boxed{+(\nu_{21}+\nu_{35})} = 512$	509
	γ_{2345}	$\nu_5 \boxed{+(\nu_{23}+\nu_{54})} = 514$	
S_9	γ_{1235}	$\nu_5 \boxed{-(\nu_{21}+\nu_{35})} = 542$	539
	γ_{2345}	$\nu_5 \boxed{-(\nu_{23}+\nu_{54})} = 540$	
S_{10}	γ_{4556}	$\nu_6 \boxed{-(\nu_{54}+\nu_{56})} = 602$	598
S_{11}	γ_{1247}	$\nu_7 \boxed{-(\nu_{21}+\nu_{47})} = 664$	665

we can focus on the optical spectra associated with modes C_2 and C_3, namely of $E_2(t)C_2(\rho,\phi)$ and $E_3(t)C_3(\rho,\phi)$ in figure 3(c). This allows us to clearly identify the emergence of the two sidebands at the mentioned locations. From these considerations, it follows that the sideband of C_2 at $\Delta\nu \approx 380$ GHz exhibit the transverse spatial profile of C_2 while the sideband of C_3 at $\Delta\nu \approx 115$ GHz reflects the spatial profile of C_3.

4. Optical spectrum sidebands

This key concept has been experimentally demonstrated, as shown in figure 4, where the near-field patterns of sidebands S_1 to S_{11} of figure 1(b) are reported. Specifically, sidebands S_2 and S_5 exhibit the spatial profiles of modes C_3 and C_2 respectively, closely matching the theoretical predictions. Table 2 lists the γ_{mnrl} coefficients alongside the predicted frequency beating values, comparing them with the experimental results extracted from figure 1(b). The close agreement between the predicted and measured values confirms the origin of these sidebands as non-null frequency beatings between modes, with the small discrepancy associated with the resolution of the OSA measurement.

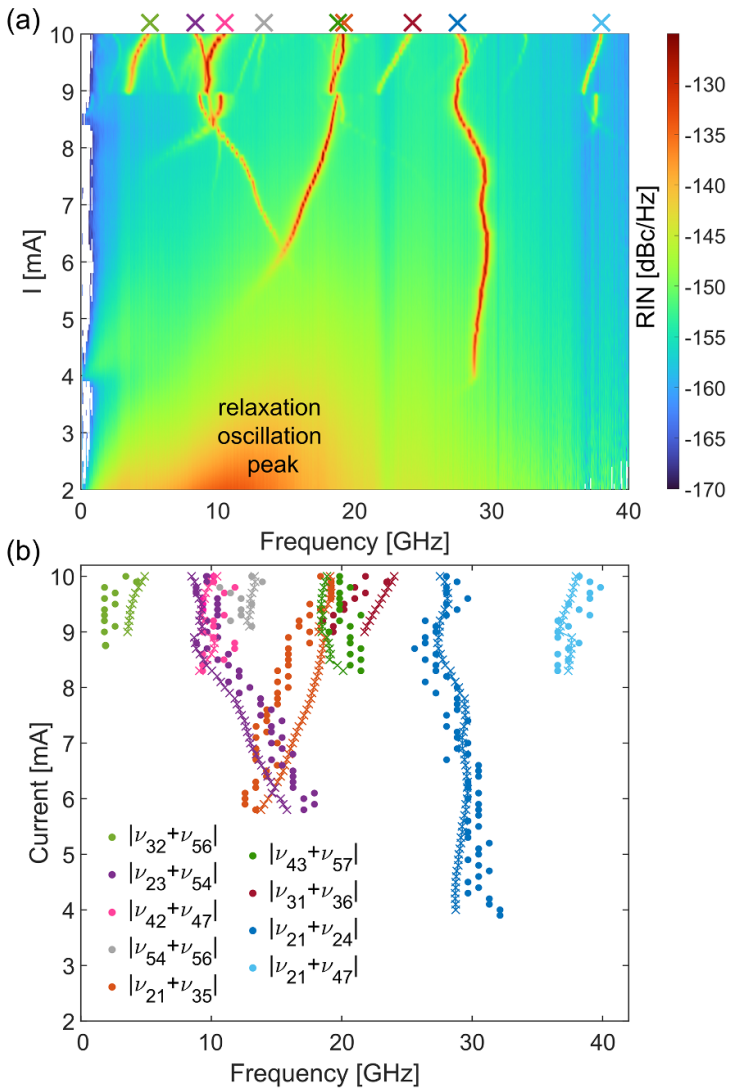

Figure 5. (a) Map of experimental RIN for varying current (y-axis). The cross markers at the top of the figure are used to label the different peaks. (b) Tracking (cross markers) of the frequency location of the RIN peaks observed in (a) and corresponding frequency beating prediction (dot markers).

Most sidebands have already been commented in the previous section. Additionally, since at 8 mA mode C_6 and C_7 are also lasing, we observe a sideband (S_{10}) of mode C_6 at a distance $|\nu_{54}+\nu_{56}|$ and a sideband of C_7 at a distance $|\nu_{21}-\nu_{47}|$.

5. Analysis of RIN peaks

Since we are limited by the OSA resolution bandwidth, the optical sidebands predicted by our model at frequencies less than 10 GHz from their mode cannot be observed in the optical spectrum. However, they are clearly visible in the measured RIN spectrum. Therefore, we need to perform RIN measurements to analyze such sidebands in detail at small beating frequencies. Moreover, frequency beatings occurring within a bandwidth of 40 GHz (and in general within the bandwidth of the receiver) are of higher importance due to their potential impact on high-speed data transmission [3].

Differently from the results in figure 4, a RIN measurement does not allow to associate the observed beating frequencies to the specific modal profiles of the involved modes. For this reason, in order to uniquely associate a peak in the RIN spectrum with a specific beating frequency, we track its frequency location for increasing bias current and compare the results with the predicted frequency, aided in the comparison by the data trends. We assume that the multimode fiber does not induce any nonlinearities and that, given its short length (1.5 m), dispersion is negligible. Therefore, since the VCSEL modes are orthonormal, such orthonormality is conserved when each VCSEL mode is projected onto a set of (orthonormal) fiber modes. As a result, the total power after the multimode fiber is simply the sum of

the powers carried by each VCSEL mode and the measured peaks in the RIN are associated only with the VCSEL physics [13].

In figure 5(a), we display a map of the measured spectral RIN as a function of the bias current (y-axis): apart from the peak associated with relaxation oscillations, prominent at small currents, we clearly observe the emergence of several peaks due to FWM starting from $I_{\text{bias}} = 4$ mA. In figure 5(b), we report the frequency location of these peaks for varying current (solid line with cross markers of the same color as the labeled peaks at the top of figure 5(a)). Instead, with dot markers, we plot the beating frequency prediction obtained with the model and calculated considering, for the frequencies of the lasing C_m modes involved, the values from the OSA measurement at the same current. While, as already discussed, the evaluation of the modal peaks made by the OSA is affected by the OSA resolution, we can clearly observe from figure 5(b) that the trend of each RIN peak is correctly predicted by our model for an increasing current.

We attribute low intensity peaks appearing around 9 mA to higher order effects, not accounted in the reduced model in equations (1)–(3). We also highlight that the 9 frequency beatings reported in figure 5 are the only ones expected from the modal competition of 7 Hermite Gaussian modes C_{1-7} (of similar detunings) in a frequency range of 40 GHz.

To conclude our analysis, we would like to qualitatively comment on the main terms impacting the RIN peak amplitude: as clearly illustrated in equation (3), the RIN peak amplitude is mainly affected by the intensity of the modal amplitudes and the saturation term E_s^2. This last term could suggest some potential mitigation strategy for the occurrence of RIN peaks within the receiver bandwidth, since the RIN peak amplitude can be reduced when E_s^2 is increased. This could be accomplished by lowering the differential gain g_N of the laser, which however would also reduce the -3 dB bandwidth of the laser. Another strategy could be to consider materials with a smaller electron decay time τ_e, which would on the other hand increase the laser threshold. Therefore, a clear path for tackling the presence of these, usually unwanted, peaks in the RIN requires a well thought balance of such effects. Another possible solution would be engineering the VCSEL oxide aperture shape such that, for proper detuning of the lasing mode, no FWM component falls within the receiver bandwidth [5].

6. Conclusions

We conducted a detailed study on the effect of transverse modal competition in an elliptical oxide aperture VCSEL with polarization control. Employing a lensed fiber near-field measurement technique, we demonstrated sidebands in the optical spectrum as the clear result of FWM, Additionally, we were able to explain in detail all high intensity peaks appearing in the RIN in presence of up to seven lasing modes. These results validate the proposed model for a proper description of coherent frequency mixing in multimode VCSELs. The deeper understanding acquired through this study paves the way for the tailoring of oxide aperture size and geometry in order to limit the effect of modal competition resulting in RIN peaks within 40 GHz, hindering for the laser performance and modulation bandwidth.

Data availability statement

The data cannot be made publicly available upon publication because they are not available in a format that is sufficiently accessible or reusable by other researchers. The data that support the findings of this study are available upon reasonable request from the authors.

Acknowledgment

The authors acknowledge Dr Fabrizio Forghieri (Cisco Photonics, Vimercate, Italy) for coordinating the project under a CISCO Sponsored Research Agreement.

Funding

This work was supported under a CISCO Sponsored Research Agreement and was partially supported by the European Union under the Italian National Recovery and Resilience Plan (PNRR) of NextGenerationEU, partnership on 'Telecommunications of the Future' (PE00000001—program 'RESTART'). CR acknowledges funding from MUQUABIS project, EU HORIZON-CL4-2021-DIGITAL-EMERGING-01, Grant Agreement N.101070546.

Author contributions

Cristina Rimoldi 0000-0001-5241-8773
Conceptualization (equal), Data curation (equal), Formal analysis (equal), Investigation (equal), Methodology (equal), Validation (equal), Visualization (equal), Writing – original draft (equal), Writing – review & editing (equal)

Marco Novarese 0000-0001-8957-469X
Conceptualization (equal), Data curation (equal), Formal analysis (equal), Investigation (equal), Methodology (equal), Validation (equal), Visualization (equal), Writing – original draft (equal), Writing – review & editing (equal)

Lorenzo Luigi Columbo 0000-0002-6566-9763
Conceptualization (equal), Formal analysis (equal), Investigation (supporting), Methodology (supporting), Supervision (supporting), Visualization (supporting), Writing – original draft (equal), Writing – review & editing (equal)

Sebastian Romero García 0000-0002-8579-3382
Investigation (supporting), Methodology (supporting), Project administration (supporting), Resources (supporting), Visualization (supporting)

Christian Raabe
Investigation (supporting), Project administration (supporting), Resources (supporting), Supervision (supporting)

Mariangela Gioannini 0000-0002-6250-5640
Conceptualization (equal), Formal analysis (supporting), Funding acquisition (equal), Investigation (supporting), Methodology (supporting), Project administration (equal), Supervision (lead), Visualization (supporting), Writing – original draft (equal), Writing – review & editing (equal)

Appendix A. Analytical form of Hermite Gaussian modes

In the following, we report the analytical form of the first 7 Hermite Gaussian modes $C_m(\rho,\phi)$, utilized for the expansion of the electric field $E(\rho,\phi,t)$ and resulting from the linear combinations of Gauss-Laguerre modes $A_{p,l}(\rho,\phi)$.

$$A_{p,l}(\rho,\phi) = \sqrt{\frac{2}{\pi}}\left(2\rho^2\right)^{|l|/2}\left[\frac{p!}{(p+|l|)!}\right]^{1/2} L_p^{|l|}\left(2\rho^2\right)\mathrm{e}^{-\rho^2}\mathrm{e}^{\mathrm{i}l\phi}$$

where p is the radial index, l is the angular index and $L_p^{|l|}(2\rho^2)$ are the Laguerre polynomials of argument $2\rho^2$.

$$\begin{aligned}
C_1(\rho,\phi) &= A_{0,0}(\rho,\phi)\\
C_2(\rho,\phi) &= \frac{1}{\sqrt{2}}\left[A_{0,1}(\rho,\phi) + A_{0,-1}(\rho,\phi)\right]\\
C_3(\rho,\phi) &= \frac{1}{\sqrt{2}i}\left[A_{0,1}(\rho,\phi) - A_{0,-1}(\rho,\phi)\right]\\
C_4(\rho,\phi) &= \frac{1}{\sqrt{3}}\left[A_{1,0}(\rho,\phi) - A_{0,2}(\rho,\phi) - A_{0,-2}(\rho,\phi)\right]\\
C_5(\rho,\phi) &= \frac{1}{\sqrt{2}i}\left[A_{0,2}(\rho,\phi) - A_{0,-2}(\rho,\phi)\right]
\end{aligned}$$

$$\begin{aligned}
C_6(\rho,\phi) &= \frac{1}{\sqrt{3}}\left[A_{1,0}(\rho,\phi) + A_{0,2}(\rho,\phi) + A_{0,-2}(\rho,\phi)\right]\\
C_7(\rho,\phi) &= \frac{1}{2}\left[A_{1,1}(\rho,\phi) + A_{1,-1}(\rho,\phi) - A_{0,3}(\rho,\phi) - A_{0,-3}(\rho,\phi)\right]
\end{aligned}$$

In a more conventional notation, $C_1 = \mathrm{TEM}_{00}$, $C_2 = \mathrm{TEM}_{01}$, $C_3 = \mathrm{TEM}_{10}$, $C_4 = \mathrm{TEM}_{02}$, $C_5 = \mathrm{TEM}_{11}$, $C_6 = \mathrm{TEM}_{20}$, $C_6 = \mathrm{TEM}_{20}$, and $C_7 = \mathrm{TEM}_{03}$.

Appendix B. Beating frequencies for 7 Hermite-Gauss modes

In table 3, we report the beating frequencies resulting from the modal competition of up to 7 Hermite Gauss modes. Squared non-zero terms may occur within a 200 GHz window for typical VCSEL with elliptical oxide aperture at most common operating currents (up to 10 mA).

Table 3. All beating frequencies for $m = 7$.

Coefficient	Angular beating frequency
γ_{1111}	0
γ_{1114}	$\pm\omega_{14}$
γ_{1116}	$\pm\omega_{16}$
γ_{1122}	$0, \pm 2\omega_{12}$
γ_{1127}	$\pm\omega_{27}, \pm(\omega_{12}+\omega_{17})$
γ_{1133}	$0, \pm 2\omega_{13}$
γ_{1144}	$0, \pm 2\omega_{14}$
γ_{1146}	$\boxed{\pm\omega_{46}}, \pm(\omega_{14}+\omega_{16})$
γ_{1155}	$0, \pm 2\omega_{15}$
γ_{1166}	$0, \pm 2\omega_{16}$
γ_{1177}	$0, \pm 2\omega_{17}$
γ_{1224}	$\boxed{\pm(\omega_{21}+\omega_{24})}, \pm\omega_{14}$
γ_{1226}	$\boxed{\pm(\omega_{21}+\omega_{26})}, \pm\omega_{16}$
γ_{1235}	$\boxed{\pm(\omega_{21}+\omega_{35})}, \pm(\omega_{12}+\omega_{35}), \pm(\omega_{13}+\omega_{25})$
γ_{1247}	$\boxed{\pm(\omega_{21}+\omega_{47})}, \pm(\omega_{12}+\omega_{47}), \pm(\omega_{14}+\omega_{27})$
γ_{1267}	$\boxed{\pm(\omega_{12}+\omega_{76})}, \boxed{\pm(\omega_{12}+\omega_{67})}, \pm(\omega_{16}+\omega_{27})$
γ_{1334}	$\boxed{\pm(\omega_{13}+\omega_{43})}, \pm\omega_{14}$
γ_{1336}	$\boxed{\pm(\omega_{31}+\omega_{36})}, \pm\omega_{16}$
γ_{1357}	$\boxed{\pm(\omega_{13}+\omega_{75})}, \pm(\omega_{13}+\omega_{57}), \pm(\omega_{15}+\omega_{37})$
γ_{1444}	$\pm\omega_{14}$
γ_{1446}	$\pm(\omega_{14}+\omega_{64}), \pm\omega_{16}$
γ_{1455}	$\pm\omega_{14}, \pm(\omega_{15}+\omega_{45})$
γ_{1466}	$\pm\omega_{14}, \pm(\omega_{16}+\omega_{46})$
γ_{1477}	$\pm\omega_{14}, \pm(\omega_{17}+\omega_{47})$
γ_{1556}	$\pm(\omega_{15}+\omega_{65}), \pm\omega_{16}$
γ_{1666}	$\pm\omega_{16}$
γ_{1677}	$\pm\omega_{16}, \pm(\omega_{17}+\omega_{67})$
γ_{2222}	0
γ_{2227}	$\pm\omega_{27}$
γ_{2233}	$0, \boxed{\pm 2\omega_{23}}$
γ_{2244}	$0, \pm 2\omega_{24}$
γ_{2246}	$\boxed{\pm\omega_{46}}, \pm(\omega_{24}+\omega_{26})$
γ_{2255}	$0, \pm 2\omega_{25}$
γ_{2266}	$0, \pm 2\omega_{26}$
γ_{2277}	$0, \pm 2\omega_{27}$
γ_{2337}	$\pm(\omega_{32}+\omega_{37}), \pm\omega_{27}$
γ_{2345}	$\boxed{\pm(\omega_{23}+\omega_{54})}, \boxed{\pm(\omega_{23}+\omega_{45})}, \pm(\omega_{24}+\omega_{35})$
γ_{2356}	$\boxed{\pm(\omega_{32}+\omega_{56})}, \boxed{\pm(\omega_{23}+\omega_{56})}, \pm(\omega_{25}+\omega_{36})$
γ_{2447}	$\boxed{\pm(\omega_{42}+\omega_{47})}, \pm\omega_{27}$
γ_{2467}	$\boxed{\pm(\omega_{24}+\omega_{76})}, \pm(\omega_{24}+\omega_{67}), \pm(\omega_{26}+\omega_{47})$
γ_{2557}	$\boxed{\pm(\omega_{25}+\omega_{75})}, \pm\omega_{27}$
γ_{2667}	$\pm(\omega_{26}+\omega_{76}), \pm\omega_{27}$
γ_{2777}	$\pm\omega_{27}$
γ_{3333}	0
γ_{3344}	$0, \pm 2\omega_{34}$
γ_{3346}	$\boxed{\pm\omega_{46}}, \pm(\omega_{34}+\omega_{36})$
γ_{3355}	$0, \pm 2\omega_{35}$

(Continued.)

Table 3. (Continued.)

Coefficient	Angular beating frequency
γ_{3366}	$0, \pm 2\omega_{36}$
γ_{3377}	$0, \pm 2\omega_{37}$
γ_{3457}	$\boxed{\pm(\omega_{43}+\omega_{57})}, \boxed{\pm(\omega_{34}+\omega_{57})}, \pm(\omega_{35}+\omega_{47})$
γ_{3567}	$\pm(\omega_{35}+\omega_{76}), \pm(\omega_{35}+\omega_{67}), \pm(\omega_{36}+\omega_{57})$
γ_{4444}	0
γ_{4446}	$\boxed{\pm\omega_{46}}$
γ_{4455}	$0, \boxed{\pm 2\omega_{45}}$
γ_{4466}	$0, \pm 2\omega_{46}$
γ_{4477}	$0, \pm 2\omega_{47}$
γ_{4556}	$\boxed{\pm(\omega_{54}+\omega_{56})}, \boxed{\pm\omega_{46}}$
γ_{4666}	$\boxed{\pm\omega_{46}}$
γ_{4677}	$\boxed{\pm\omega_{46}}, \pm(\omega_{47}+\omega_{67})$
γ_{5555}	0
γ_{5566}	$0, \boxed{\pm 2\omega_{56}}$
γ_{5577}	$0, \pm 2\omega_{57}$
γ_{6666}	0
γ_{6677}	$0, \boxed{\pm 2\omega_{67}}$
γ_{7777}	0

References

[1] Michalzik R 2013 *VCSELs* (Springer) (available at: https://doi.org/10.1007/978-3-642-24986-0)
[2] Chaqmaqchee F A I and Lott J A 2020 Impact of oxide aperture diameter on optical output power, spectral emission and bandwidth for 980 nm VCSELs *OSA Contin.* **3** 2602–13
[3] Huang K-Y, Weng J-H, Wang J, Chang-Hasnain C J and Lin G-R 2024 Anomalous noise spikes beating from a fine-splitting mode of surface-emitting laser with imperfect true-roundness aspect *Photon. Res.* **12** 2957–71
[4] Quirce A, Valle A, Giménez C and Pesquera L 2011 Intensity noise characteristics of multimode VCSELs *J. Lightwave Technol.* **29** 1039–45
[5] Rimoldi C, Columbo L L, Tibaldi A, Debernardi P, García S R, Raabe C and Gioannini M 2025 Impact of coherent mode coupling on noise performance in elliptical aperture VCSELs for datacom *IEEE J. Sel. Top. Quantum Electron.* **31** 1–13
[6] Bittner S and Sciamanna M 2022 Complex nonlinear dynamics of polarization and transverse modes in a broad-area VCSEL *APL Photonics* **7** 126108
[7] Debernardi P, Ostermann J M, Sondermann M, Ackemann T, Bava G P and Michalzik R 2007 Theoretical-experimental study of the vectorial modal properties of polarization-stable multimode grating VCSELs *IEEE J. Sel. Top. Quantum Electron.* **13** 1340–8
[8] Gazula D, Chitica N, Chacinski M, Landry G and Tatum J 2019 VCSEL with elliptical aperture having reduced RIN *US Patent* 20190341743A1
[9] Debernardi P, Bava G, Degen C, Fischer I and Elsasser W 2002 Influence of anisotropies on transverse modes in oxide-confined VCSELs *IEEE J. Quantum Electron.* **38** 73–84
[10] Solomon C and Breckon T 2010 *Image Restoration* (Wiley) ch 6, pp 141–67
[11] Gonzalez R C and Woods R E 1992 *Digital Image Processing* (Addison-Wesley Publishing Company, Inc.)
[12] Lam E Y and Goodman J W 2000 Iterative statistical approach to blind image deconvolution *J. Opt. Soc. Am. A* **17** 1177–84
[13] Li S, Nezami M S, Mishra S and Liboiron-Ladouceur O 2021 Spectral-dependent electronic-photonic modeling of high-speed VCSEL-MMF links for optimized launch conditions *Opt. Express* **29** 2738–56